

Within this reconstruction-based quantification (RBQ) framework, dual-isotope reconstruction approaches provide a mechanism to jointly reconstruct the ^{227}Th and ^{223}Ra distributions. These existing approaches can be divided into two categories. The first category compensates for the crosstalk contamination between the two isotopes prior to performing reconstruction [12]–[15]. A widely used approach in this category is triple energy window (TEW)-based crosstalk compensation, which assumes that crosstalk contamination arises mainly from scattered photons [12]. However, in the joint ^{227}Th and ^{223}Ra quantification, due to the highly overlapped emission spectra, crosstalk contamination is also caused by primary photons, which is challenging to compensate with the TEW-based method. In addition, the TEW method typically obtains noisy crosstalk estimates from narrow energy windows positioned on either side of the photopeak window. Compensation using these noisy crosstalk estimates leads to amplified image noise [16], [17]. The second category of methods performs model-based crosstalk compensation during reconstruction [16], [18]–[23]. These methods can be designed to model crosstalk from both primary and scattered photons, and they have recently been studied for jointly quantifying ^{227}Th and ^{223}Ra activity uptake [24]. However, at low counts, these RBQ approaches have been observed to yield limited accuracy and precision, with bias and standard deviation values between 10-35% and 12-30%, respectively, even with finely tuned reconstruction protocols [24]–[28]. Thus, there is an important need for new approaches to jointly quantify the uptake of ^{227}Th and ^{223}Ra .

The major challenge in RBQ methods is the requirement to estimate many voxel values, which is challenging at low count levels. To address this inherent limitation, building upon ideas proposed by Carson [29], we developed a single-isotope projection-domain low-count quantitative SPECT (LC-QSPECT) method that directly estimates activity uptake in the VOIs [25]. The method was validated for ^{223}Ra -based α -RPTs, and observed to yield accurate and precise regional uptake estimates and outperform conventional RBQ methods [25]. To further address the issue of low counts, we recognize that both ^{227}Th and ^{223}Ra emit γ -ray photons over multiple photopeak energies. Recent studies have shown that using measurements from multiple energy windows can help improve quantification performance [30], [31]. Further, using photons from multiple energy windows corresponding to these different photopeaks provides a mechanism to increase the photon counts and thus improve the effective system sensitivity [26]. Integrating these ideas, we propose a multiple-energy-window projection-domain quantification (MEW-PDQ) method that jointly estimates the regional activity uptake of ^{227}Th and ^{223}Ra directly from low-count SPECT projections acquired over multiple energy windows. Preliminary versions of the work described in this paper have been presented previously [32], [33].

II. THEORY

Consider a SPECT system that images a radioisotope distribution of both ^{227}Th and ^{223}Ra . Both ^{227}Th and ^{223}Ra emit

photons at multiple energies. Denote the overall γ -ray source distribution as $\Xi(\mathbf{r}, \mathcal{E})$, which describes the mean emission rate of γ -ray photons with energy \mathcal{E} at the 3-dimensional (3D) position \mathbf{r} . Denote the measured projection data by a M -dimensional vector \mathbf{g} , containing projections in multiple energy windows. Denote the number of projection bins with different spatial positions by M_s , and the number of energy windows by M_e . Thus, $M = M_s \times M_e$.

Assume that the γ -ray source distribution being imaged and the projection data lie in the Hilbert space of square-integrable functions, denoted by $\mathbb{L}_2(\mathbb{R}^4)$, and the Hilbert space of Euclidean vectors, denoted by \mathbb{E}^M , respectively. Then, the SPECT system imaging the γ -ray source distribution, denoted by the operator \mathcal{H} , can be described as an integral transform from $\mathbb{L}_2(\mathbb{R}^4)$ to \mathbb{E}^M . Denote the kernel of the \mathcal{H} operator by $h_m(\mathbf{r}, \mathcal{E})$, which describes the sensitivity of the m^{th} element of projection \mathbf{g} to a γ -ray photon emitted at position \mathbf{r} with energy \mathcal{E} .

In SPECT with α -RPTs, due to the very low count levels, the stray-radiation-related noise due to photons emitted from regions other than the patient forms a substantial portion of the measured counts. We model this noise as Poisson distributed, with the same mean for all projection bins in a given energy window but different means for different energy windows. Let Ψ be an M -dimensional vector that denotes the mean stray-radiation-related noise in the M projection bins. The imaging system equation is given by

$$\mathbf{g} = \mathcal{H}\Xi + \Psi + \mathbf{n} \quad (1)$$

where \mathbf{n} , an M -dimensional vector, denotes the entire noise in the imaging system. Overall, the data \mathbf{g} is Poisson distributed with mean of $\mathcal{H}\Xi + \Psi$. The m^{th} element of this vector is given by:

$$g_m = \int \int h_m(\mathbf{r}, \mathcal{E}) \Xi(\mathbf{r}, \mathcal{E}) d^3r d\mathcal{E} + \psi_m + n_m. \quad (2)$$

The term $\Xi(\mathbf{r}, \mathcal{E})$ comprises γ -rays emitted by both ^{227}Th and ^{223}Ra . Denote the mean emission rate of γ -ray photons from ^{227}Th and ^{223}Ra with energy \mathcal{E} at position \mathbf{r} by $\Xi^{Th}(\mathbf{r}, \mathcal{E})$ and $\Xi^{Ra}(\mathbf{r}, \mathcal{E})$, respectively. Then

$$\Xi(\mathbf{r}, \mathcal{E}) = \Xi^{Th}(\mathbf{r}, \mathcal{E}) + \Xi^{Ra}(\mathbf{r}, \mathcal{E}). \quad (3)$$

Since the emission rates of γ -ray photons with different energies are independent of the spatial location, we can decompose $\Xi^{Th}(\mathbf{r}, \mathcal{E})$ and $\Xi^{Ra}(\mathbf{r}, \mathcal{E})$ as

$$\Xi^{Th}(\mathbf{r}, \mathcal{E}) = f^{Th}(\mathbf{r}) \zeta^{Th}(\mathcal{E}), \quad (4a)$$

$$\Xi^{Ra}(\mathbf{r}, \mathcal{E}) = f^{Ra}(\mathbf{r}) \zeta^{Ra}(\mathcal{E}), \quad (4b)$$

where $\zeta^{Th}(\mathcal{E})$ and $\zeta^{Ra}(\mathcal{E})$ describe the mean emission rates of γ -ray photons with energy \mathcal{E} from a unit activity of ^{227}Th and ^{223}Ra , respectively, and $f^{Th}(\mathbf{r})$ and $f^{Ra}(\mathbf{r})$ denote the spatial distribution of these isotopes. Inserting Eqs. (3) and (4) into Eq. (2), we obtain

$$g_m = \int f^{Th}(\mathbf{r}) \int h_m(\mathbf{r}, \mathcal{E}) \zeta^{Th}(\mathcal{E}) d\mathcal{E} d^3r + \int f^{Ra}(\mathbf{r}) \int h_m(\mathbf{r}, \mathcal{E}) \zeta^{Ra}(\mathcal{E}) d\mathcal{E} d^3r + \psi_m + n_m. \quad (5)$$

We define

$$h_m^{Th}(\mathbf{r}) = \int h_m(\mathbf{r}, \mathcal{E}) \zeta^{Th}(\mathcal{E}) d\mathcal{E}, \quad (6a)$$

$$h_m^{Ra}(\mathbf{r}) = \int h_m(\mathbf{r}, \mathcal{E}) \zeta^{Ra}(\mathcal{E}) d\mathcal{E}. \quad (6b)$$

The terms $h_m^{Th}(\mathbf{r})$ and $h_m^{Ra}(\mathbf{r})$ can be considered as kernels of two isotope-dependent system operators, describing the sensitivity of the m^{th} element of \mathbf{g} to a unit activity uptake of ^{227}Th and ^{223}Ra at position \mathbf{r} , respectively. Eq. (5) can be written as

$$g_m = \int \{h_m^{Th}(\mathbf{r})f^{Th}(\mathbf{r}) + h_m^{Ra}(\mathbf{r})f^{Ra}(\mathbf{r})\} d^3r + \psi_m + n_m. \quad (7)$$

In Eq. (7), we defined the imaging equation in terms of the spatial distribution of $f^{Th}(\mathbf{r})$ and $f^{Ra}(\mathbf{r})$. We recognize that our objective is to estimate the absolute regional activity uptake of both isotopes within a set of VOIs. Mathematically, we first define a 3D VOI function $\phi_k^{VOI}(\mathbf{r})$, where

$$\phi_k^{VOI}(\mathbf{r}) = \begin{cases} 1, & \text{if } \mathbf{r} \text{ lies within the } k^{\text{th}} \text{ VOI.} \\ 0, & \text{otherwise.} \end{cases} \quad (8)$$

Denote $\boldsymbol{\lambda}^{Th}$ and $\boldsymbol{\lambda}^{Ra}$ as K -dimensional vectors of regional uptake of ^{227}Th and ^{223}Ra , respectively. λ_k^{Th} and λ_k^{Ra} are given by

$$\lambda_k^{Th} = \frac{\int d^3r f^{Th}(\mathbf{r})\phi_k^{VOI}(\mathbf{r})}{\int d^3r \phi_k^{VOI}(\mathbf{r})}, \quad (9a)$$

$$\lambda_k^{Ra} = \frac{\int d^3r f^{Ra}(\mathbf{r})\phi_k^{VOI}(\mathbf{r})}{\int d^3r \phi_k^{VOI}(\mathbf{r})}, \quad (9b)$$

respectively. Our objective is to estimate $\boldsymbol{\lambda}^{Th}$ and $\boldsymbol{\lambda}^{Ra}$.

Toward this goal, we directly represent the activity uptake distributions $f^{Th}(\mathbf{r})$ and $f^{Ra}(\mathbf{r})$ in terms of the VOI-basis functions as given by Eq. (8). The activity distributions of ^{227}Th and ^{223}Ra are then represented in terms of these basis functions as

$$f_{VOI}^{Th}(\mathbf{r}) = \sum_{k=1}^K \lambda_k^{Th} \phi_k^{VOI}(\mathbf{r}), \quad (10a)$$

$$f_{VOI}^{Ra}(\mathbf{r}) = \sum_{k=1}^K \lambda_k^{Ra} \phi_k^{VOI}(\mathbf{r}), \quad (10b)$$

respectively. Inserting the VOI-based representations for $f^{Th}(\mathbf{r})$ and $f^{Ra}(\mathbf{r})$ in Eq. (7) yields the following expression for the m^{th} element of the vector \mathbf{g}

$$g_m = \sum_{k=1}^K \lambda_k^{Th} \int h_m^{Th}(\mathbf{r})\phi_k^{VOI}(\mathbf{r}) d^3r + \sum_{k=1}^K \lambda_k^{Ra} \int h_m^{Ra}(\mathbf{r})\phi_k^{VOI}(\mathbf{r}) d^3r + \psi_m + n_m. \quad (11)$$

To simplify the notation, we define \mathbf{H}^{Th} and \mathbf{H}^{Ra} as two $M \times K$ dimensional system matrices with elements given by

$$H_{mk}^{Th} = \int d^3r h_m^{Th}(\mathbf{r})\phi_k^{VOI}(\mathbf{r}), \quad (12a)$$

$$H_{mk}^{Ra} = \int d^3r h_m^{Ra}(\mathbf{r})\phi_k^{VOI}(\mathbf{r}), \quad (12b)$$

respectively. Then, Eq. (11) can be written as

$$g_m = \sum_{k=1}^K H_{mk}^{Th} \lambda_k^{Th} + \sum_{k=1}^K H_{mk}^{Ra} \lambda_k^{Ra} + \psi_m + n_m. \quad (13)$$

This can be then written in vector form as

$$\mathbf{g} = \mathbf{H}^{Th} \boldsymbol{\lambda}^{Th} + \mathbf{H}^{Ra} \boldsymbol{\lambda}^{Ra} + \boldsymbol{\Psi} + \mathbf{n}. \quad (14)$$

To make the notation more concise, we define the following terms:

$$\mathbf{H} = [\mathbf{H}^{Th} \quad \mathbf{H}^{Ra}], \quad \boldsymbol{\lambda} = \begin{bmatrix} \boldsymbol{\lambda}^{Th} \\ \boldsymbol{\lambda}^{Ra} \end{bmatrix}. \quad (15)$$

Then, Eq. (14) can be written as

$$\mathbf{g} = \mathbf{H} \boldsymbol{\lambda} + \boldsymbol{\Psi} + \mathbf{n}. \quad (16)$$

Having derived this mathematical formalism to estimate $\boldsymbol{\lambda}$, we derive a maximum-likelihood (ML) expectation maximization (EM) approach. Denote the probability of a discrete random variable x as $\text{Pr}(x)$. Then the probability of the measured projection data is given by

$$\text{Pr}(\mathbf{g}|\boldsymbol{\lambda}) = \prod_{m=1}^M \text{Pr}(g_m|\boldsymbol{\lambda}), \quad (17)$$

where we have used the fact that the measured data across the different bins and energy windows are independent. Now, from Eq. (16), the measured data g_m is Poisson distributed with mean $(\mathbf{H}\boldsymbol{\lambda})_m + \psi_m$. Thus

$$\begin{aligned} \text{Pr}(\mathbf{g}|\boldsymbol{\lambda}) &= \prod_{m=1}^M \exp[-(\mathbf{H}^{Th} \boldsymbol{\lambda}^{Th} + \mathbf{H}^{Ra} \boldsymbol{\lambda}^{Ra})_m - \psi_m] \\ &\times \frac{[(\mathbf{H}^{Th} \boldsymbol{\lambda}^{Th} + \mathbf{H}^{Ra} \boldsymbol{\lambda}^{Ra})_m + \psi_m]^{g_m}}{g_m!}. \end{aligned} \quad (18)$$

This gives the likelihood of the measured data \mathbf{g} . To estimate $\boldsymbol{\lambda}$, we maximize the logarithm of this likelihood of $\boldsymbol{\lambda}$ given \mathbf{g} . Briefly, we differentiate the log-likelihood with respect to the elements of $\boldsymbol{\lambda}$ and equate that to 0 to find the point at which the log-likelihood is maximized. This yields the following coupled equations to estimate the regional activity uptake of ^{227}Th and ^{223}Ra in the k^{th} VOI:

$$\widehat{\lambda}_k^{Th(t+1)} = \frac{\widehat{\lambda}_k^{Th(t)}}{\sum_{m=1}^M H_{mk}^{Th}} \sum_{m=1}^M \frac{g_m}{[\mathbf{H}\widehat{\boldsymbol{\lambda}}^{(t)}]_m + \psi_m} H_{mk}^{Th}, \quad (19a)$$

$$\widehat{\lambda}_k^{Ra(t+1)} = \frac{\widehat{\lambda}_k^{Ra(t)}}{\sum_{m=1}^M H_{mk}^{Ra}} \sum_{m=1}^M \frac{g_m}{[\mathbf{H}\widehat{\boldsymbol{\lambda}}^{(t)}]_m + \psi_m} H_{mk}^{Ra}, \quad (19b)$$

where $\widehat{\lambda}_k^{Th(t)}$ and $\widehat{\lambda}_k^{Ra(t)}$ denote the estimates of λ_k^{Th} and λ_k^{Ra} in the t^{th} iteration.

The proposed MEW-PDQ method has several advantages. First, the method makes use of projection data from multiple energy windows. This not only improves the effective system sensitivity but can also improve the theoretical limits of precisely estimating the uptake [31]. Second, the number of

VOIs, K , is lower than the number of voxels reconstructed in the image RBQ approaches, so the problem is less ill-posed. Next, the method is less sensitive to partial volume effects (PVEs) [34], a major degrading effect in image reconstruction-based QSPECT. PVEs arise due to two factors, the first being the finite system resolution, and the second being the pixelized representation of a continuous object (tissue-fraction effects). The proposed method is less affected by both these factors since we define the boundaries of VOIs before estimating the regional uptake and since there are no voxelizations. A final advantage is that we directly estimate the regional uptake from the projection data, this avoids reconstruction-related information loss [35], [36].

III. IMPLEMENTATION AND EVALUATION OF THE PROPOSED METHOD

A. Implementation

To implement the proposed MEW-PDQ method, we first need to obtain the elements of the system matrices corresponding to imaging ^{227}Th and ^{223}Ra , as shown in Eqs. (12a) and (12b), respectively. We used a Monte Carlo (MC)-based approach to obtain these elements. Specifically, we used SIMIND, a well-validated MC-based simulation software [37]–[39]. For each isotope, we modeled the entire emission spectrum that contained γ -ray photons with different energies, emitted at each step of the decay chain. Next, we defined the VOIs for a given patient. The VOIs can be obtained by segmenting the X-ray CT acquired in conjunction with the SPECT. For each isotope, we assigned unit activity uptake to the VOI mask and zero uptake elsewhere. Assuming that the attenuation map of the whole patient was available, using SIMIND, we generated the projection of this activity map. For each isotope and for each VOI, we simulated more than 500 million decay events to ensure a low Poisson noise in the generated projection. As suggested in [6], to cover the major photopeaks of both isotopes, we considered the detection of photons in four energy windows (Fig. 1). The simulations modeled all relevant image-degrading processes in SPECT, including the attenuation, scatter, collimator response, septal penetration and scatter, characteristic X-ray from both the α -emitting isotopes and the lead in the collimator, finite energy and position resolution of the detector, and the backscatter in the detector. The energy dependency of these image-degrading processes was also modeled. Normalizing the projection data yielded the corresponding column of the system matrix for each isotope.

Next, we obtained the values of mean stray-radiation-related noise ψ_m in Eqs. (19a) and (19b). The mean of this noise in energy window 3 (Fig. 1) was determined from a planar blank scan acquired on an actual SPECT system for 10 minutes. Averaging the counts in projection bins in the corresponding energy window of this scan yielded the mean background counts for 10 minutes, which were then scaled according to the acquisition time of patient images to estimate the mean of stray-radiation-related noise in this energy window. The mean values of the stray-radiation-related noise for the other energy windows in Fig. 1 were estimated by scaling the mean of

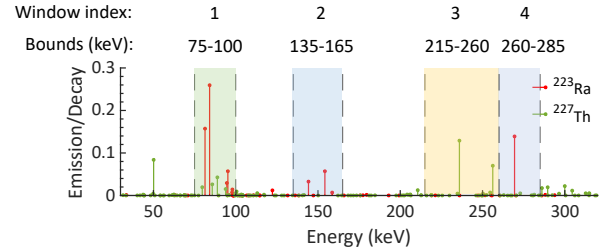


Fig. 1: Bounds of different energy windows and γ -ray emission spectra of ^{227}Th and ^{223}Ra .

energy window 3 by the relative width of the corresponding energy window. We assumed here that the mean values of stray-radiation-related noise were proportional to the widths of the energy windows. The computed system matrix and means of stray-radiation-related noise were used in Eqs. (19a) and (19b) to estimate the regional uptake directly from the projection data. The process to generate the system matrix and simulate the noise was validated by comparing the data generated using our simulation process to the measured data on an actual SPECT scanner. Details of this validation are provided in the Supplementary material as well as in Li et al. [40].

B. Evaluation framework

Evaluating the performance of the MEW-PDQ method required a setup where the ground-truth regional uptake is known. For this purpose, we conducted realistic simulation-based studies, including a virtual imaging trial (VIT). These simulations were conducted in the context of imaging patients with bone metastases of prostate cancer who were treated with ^{227}Th -based α -RPTs. We focused on lesions in the pelvis, a major site of osseous metastases, located near the prostate.

1) *Generating the patient phantom*: We used the Extended Cardiac-Torso (XCAT) phantom to generate realistic digital 3D activity and attenuation maps of patient torsos [41]. To simulate continuously distributed activities and attenuation coefficients, we considered high-resolution activity and attenuation maps, namely 512×512 along the axial dimension and 364 slices along the depth dimension, with voxel side length of 1.105 mm. Each patient had an identically located lesion in the pelvic bone. Based on our analysis of clinical SPECT of patients administered ^{223}Ra therapy, the lesion, bone, and gut are the three primary sites of uptake [25]. The rest of the region in the patient typically has a similar and low uptake, which we refer to as the background. Based on this observation, we assumed that the activity uptake distribution of ^{227}Th would have a similar pattern across these four VOIs. The heights, weights, lesions sizes, and activity uptake distributions of ^{227}Th and ^{223}Ra of the simulated patients were specific to each experiment, as we will describe in Sec. III-C.

2) *Modeling the SPECT system*: We simulated the scenario where the torso region of a patient was imaged for 30 minutes using a dual-head GE Discovery 670 SPECT/CT system with a high energy general purpose (HEGP) collimator. The simulations were performed with SIMIND. The intrinsic spatial

and energy resolution of the scintillation detector in the system were 3.9 mm and 9.8 % at 140 keV, respectively. Projections were acquired in four energy windows, as indicated in Fig. 1, and at 60 angular positions spaced uniformly over 360° . We simulated the emission spectra of both isotopes, the stray-radiation-related noise, and all relevant image-degrading processes in SPECT. In the following sections, each instance of SPECT projection generated for a simulated patient is referred to as a noise realization.

3) *Estimating the uptake using the proposed method and other compared methods:* We quantified the regional uptake from the simulated projections using the proposed method as described in Sec. III-A and, for comparison, with two state-of-art RBQ methods: a dual-isotope ordered subset expectation maximization (DOSEM)-based RBQ method similar to that proposed in [24] and the DOSEM method with geometric transfer matrix (GTM)-based PVE compensation [42]. These methods were specifically designed and optimized for the joint ^{227}Th and ^{223}Ra quantification problem. Implementation details of the DOSEM and GTM-based methods are provided in the Supplementary material as well as in Li et al. [40].

4) *Figures of merit:* We evaluated the accuracy, precision, and overall error of the considered methods on the task of estimating regional uptake. When the goal was to quantify performance over multiple noise realizations with a single patient, normalized bias (NB), normalized standard deviation (NSD), and normalized root mean square error (NRMSE) were used to quantify the accuracy, precision, and overall error, respectively. To evaluate the accuracy and overall error of these methods over a patient population, we used ensemble NB and ensemble NRMSE. Finally, our results indicated that the proposed method was almost unbiased. Thus, we compared the NSD of the estimates obtained with the proposed method with the square root of the Cramér-Rao lower bound (CRLB) normalized by the ground truth uptake (referred to as the CRLB-derived NSD). Note that the CRLB is the minimum variance that can be achieved by an unbiased estimator. Details on calculating the figures of merit are provided in the Supplementary material as well as in Li et al. [40].

C. Experiments

In this section, we describe the experiments we conducted to assess the performance of the proposed MEW-PDQ method under different experimental conditions and to evaluate the impact of using multiple energy windows on the precision of the method.

1) *Evaluating the convergence of the MEW-PDQ method:* In this experiment, the simulated patients had the same height and weight as a 50th percentile male adult in the US [41], which we refer to as average patient size. The patient torsos contained a total of 11 MBq activity of both ^{227}Th and ^{223}Ra , referred to as standard total uptake. The regional uptake ratios of the two isotopes in the four VOIs of the patients are shown in Table I. Based on the analysis of the clinical SPECT of patients receiving ^{223}Ra therapy, these values were chosen to simulate the differences in uptake in different VOIs. The convergence of the proposed method was evaluated for lesions

TABLE I: Activity uptake ratios of ^{227}Th and ^{223}Ra in VOIs, simulating the difference in regional uptake and independent biodistribution of the two isotopes.

	Background	Bone	Gut	Lesion
^{223}Ra	2	5	25	20
^{227}Th	12	30	100	300

with different diameter values. We simulated three patients, each had a lesion with diameters: 15 mm, 25 mm, and 35 mm, respectively. We generated one noise realization for each patient, as described in Sec. III-B.2, then applied the MEW-PDQ method for 1500 iterations, and computed the error in the estimated lesion uptake for both isotopes after every 50 iterations for each patient.

2) *Evaluating performance as a function of lesion size and contrast:* Following procedures similar to that described in Sec. III-C.1, we generated five patient phantoms. Each patient had a lesion diameter ranging from 15 mm to 35 mm in 5 mm increments. Then, to evaluate the sensitivity of the method to the lesion-to-bone uptake ratio (LBUR), we generated five more patient phantoms with average patient size and standard total uptake. Each patient had a lesion with a diameter of 33.75 mm, the average lesion diameter derived from clinical data [43]. Each patient had a different LBUR for both isotopes, ranging from 2:1 to 6:1, while the activity uptake ratios in the background, bone, and gut regions are shown in Table I. We generated 100 noise realizations for each patient.

3) *Evaluating performance with different ^{227}Th to ^{223}Ra uptake ratios:* In dosimetry studies, typically, the patients are imaged at multiple time points post-administration. The ^{227}Th to ^{223}Ra uptake ratio in the patient changes over time due to the decay of both isotopes. Thus, it is important to evaluate the performance of the methods for different ^{227}Th to ^{223}Ra uptake ratio values. We simulated the scenario where a patient with average patient size and a 33.75 mm diameter lesion was initially administered with 11 MBq ^{227}Th activity and was imaged at 67, 139, 243, 672 h after administration, leading to ^{227}Th to ^{223}Ra uptake ratios of 10:1, 5:1, 3:1, and 1:1, respectively. We considered both the decay of ^{227}Th and ^{223}Ra , but the organ-specific half-life of the isotopes in the patient was not modeled. Thus, for each isotope, the ratios of uptake among different VOIs remained the same as indicated in Table I. For each ^{227}Th to ^{223}Ra uptake ratio, we generated 100 noise realizations of the patient.

4) *Evaluating sensitivity to spatial intra-lesion heterogeneity:* In contrast to the DOSEM-based method, the MEW-PDQ method directly estimates the mean regional uptake from the projection data, without accounting for the potential heterogeneous activity uptake in the VOI [44], [45]. The objective of this experiment was to assess the impact that intra-lesion heterogeneity may have on the proposed method.

We generated five patient phantoms with average patient size, standard total uptake, and regional uptake ratios as shown in Table I. Each patient had a 33.75 mm diameter lesion with the same mean uptake but a different amount of spatial intra-lesion uptake heterogeneity. This heterogeneity was quantified using entropy, where a higher entropy value indicates higher

heterogeneity. To simulate this heterogeneity, we modeled the uptake in the lesion as a 3D lumpy model [46], following a similar process as described in [25]. The generated lesions and the corresponding entropy values are shown in Fig. 6a. Again, 100 noise realizations were generated for each patient.

5) *Evaluating the impact of using multiple energy windows on the precision of the proposed method:* To quantitatively assess the impact of using multiple energy windows on the theoretical lower bound of the estimated regional uptake variance using the proposed method, we computed the CRLB for the estimates with different numbers of energy windows. For this purpose, we first generated a patient phantom with the average patient size, a 33.75 mm diameter lesion, standard total uptake, and regional uptake ratios as shown in Table I. Calculating the CRLB for the estimated uptake with different numbers of energy windows requires the corresponding system matrix of the patient. We considered four energy window ranges: single window 1, windows 1-2, windows 1-3, and windows 1-4, as depicted in Fig. 1. The system matrices of the patient with the four energy window ranges were generated for both isotopes, as described in Sec. III-A. The corresponding CRLB-derived NSD values were then calculated.

As shown in the results presented later (Fig. 7), the CRLB was the lowest when data from all four energy windows were used. To evaluate if the MEW-PDQ method could yield estimates with variances that approach this lowest theoretical limit for all VOIs, we generated 100 noise realizations of the patient phantom described above in this section. With each noise realization, the MEW-PDQ method was applied to estimate the mean regional uptake of both ^{223}Ra and ^{227}Th from projections in all four energy windows (Fig. 1). The NSDs of these estimates were compared to the CRLB-derived NSD values with all these four energy windows.

6) *Evaluating performance in a simulated clinical scenario using a virtual imaging trial (VIT):* VITs provide a rigorous and objective mechanism to evaluate the performance of new imaging technologies in simulated clinical scenarios that model patient population variability [47]. In our VIT, we simulated 60 realistic patients with various body sizes, lesions diameters, and regional uptake ratios. The heights and weights of the patients were sampled from a Gaussian distribution, with the mean equal to the height and weight of a 50th percentile male US adult, with a 10% standard deviation. Next, based on clinically derived parameters [43], the lesion diameter was sampled from a Gaussian distribution with a mean of 33.75 mm and a standard deviation of 12.64 mm. We simulated a scenario where the patients were initially administered with 11 MBq activity of ^{227}Th and imaged 139 h after administration, when the ^{227}Th to ^{223}Ra uptake ratio in the patient was on average approximately 5:1. The activity uptake of both isotopes in the four VOIs were sampled independently from a normal distribution, with the mean regional uptake ratios shown in Table I and a 10% standard deviation. We generated a single noise realization for each simulated patient.

IV. RESULTS

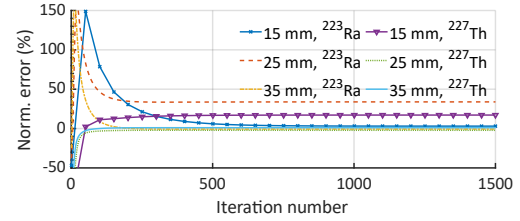


Fig. 2: Normalized error in the estimated lesion uptake of ^{227}Th and ^{223}Ra with different lesion diameters as a function of the number of iterations, showing the convergence of the MEW-PDQ method.

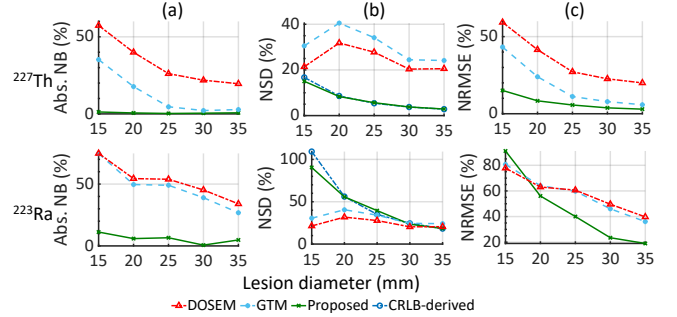


Fig. 3: The (a) absolute NB, (b) NSD, and (c) NRMSE of the estimated lesion uptake of ^{227}Th and ^{223}Ra as a function of lesion diameter.

A. Convergence of the proposed method

Fig. 2 shows the normalized error in the estimated lesion uptake of ^{227}Th and ^{223}Ra as a function of the number of iterations of the MEW-PDQ method. The method converged after 1000 iterations for both isotopes and all three lesion diameters. Thus, we chose 1000 as the number of iterations for subsequent experiments using the MEW-PDQ method.

B. Quantitation performance as a function of lesion size and contrast

The absolute NB, NSD, and NRMSE of the estimated lesion uptake as a function of lesion diameter and LBUR are shown in Figs. 3 and 4, respectively. We also compared the NSD of the estimates with CRLB-derived NSD values. For both ^{227}Th and ^{223}Ra in lesions with all diameters and LBURs, the MEW-PDQ method consistently yielded close to zero bias and an NSD close to that derived from the CRLB. The proposed method also generally outperformed the DOSEM and GTM-based methods regardless of the lesion diameters or the LBURs.

C. Quantitation performance for different ^{227}Th to ^{223}Ra uptake ratios

Fig. 5 shows the absolute NB, NSD, and NRMSE of the estimated lesion uptake for different ^{227}Th to ^{223}Ra uptake ratios. For all ^{227}Th to ^{223}Ra uptake ratios, the MEW-PDQ method consistently yielded almost zero NB and an NSD close to the CRLB-derived NSD value. In contrast, the estimates from the DOSEM and GTM-based methods had a

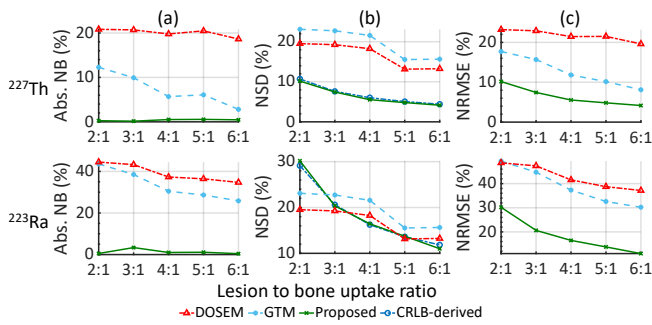


Fig. 4: The (a) absolute NB, (b) NSD, and (c) NRMSE of the estimated lesion uptake of ^{227}Th and ^{223}Ra as a function of lesion-to-bone uptake ratio.

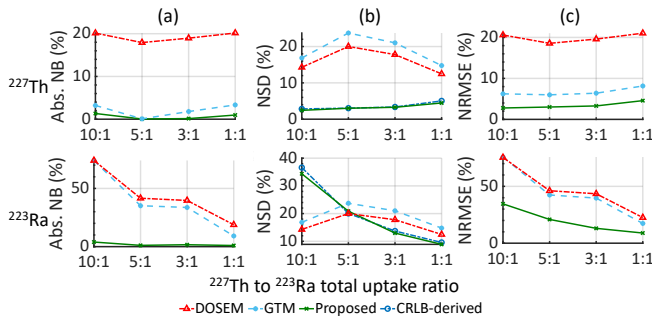


Fig. 5: The (a) absolute NB (b) NSD, and (c) NRMSE of the estimated lesion uptake of ^{227}Th and ^{223}Ra as a function of ^{227}Th to ^{223}Ra uptake ratio.

significantly higher overall error for all levels of mixtures of ^{227}Th and ^{223}Ra .

D. Sensitivity to spatial intra-lesion heterogeneity

Fig. 6 b and c show the absolute NB and NRMSE of the estimated lesion uptake for different degrees of spatial intra-lesion heterogeneity (as quantified with entropy) using the MEW-PDQ, DOSEM, and GTM-based methods. The MEW-PDQ method consistently yielded low bias in estimated regional uptake for all degrees of heterogeneity. Interestingly, despite the voxelization-derived spatial information provided through the reconstruction-based DOSEM and GTM-based methods, we observe that the proposed method yielded superior performance in terms of the overall error to either of these methods on the task of estimating regional uptake.

E. Impact of using multiple energy windows on the precision of estimates

Fig. 7 shows the CRLB-derived NSDs with different numbers of energy windows. The CRLB-derived NSD decreased with an increase in the number of energy windows. Compared with using only the first energy window, using all four windows led to at least a 58% decrease in the CRLB-derived NSD values for all regions and isotopes.

Fig. 8 compares the NSD of the estimated regional uptake of ^{227}Th and ^{223}Ra with projections in all four energy windows using the MEW-PDQ method with the CRLB-derived NSDs.

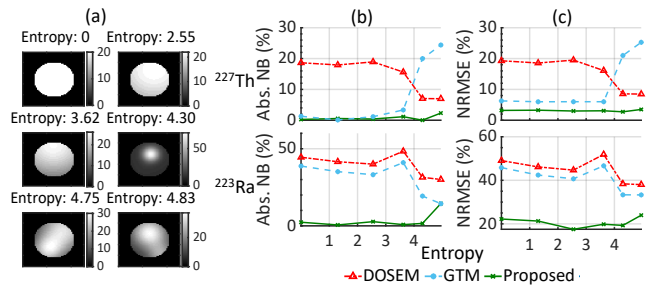


Fig. 6: The (a) activity map of lesions with multiple levels of intra-lesion heterogeneity. The (b) absolute NB, and (c) NRMSE of the estimated lesion uptake of ^{227}Th and ^{223}Ra .

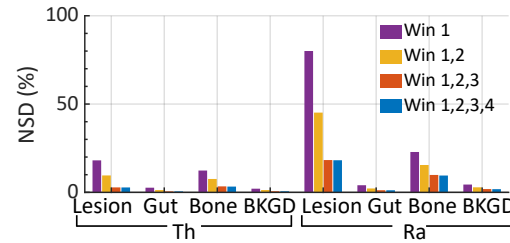


Fig. 7: Comparing the CRLB-derived NSDs of the estimated regional uptake of ^{227}Th and ^{223}Ra , for different numbers of energy windows in the MEW-PDQ method.

For all regions and isotopes, the proposed method yielded an NSD very close to that derived from the CRLB.

F. Virtual imaging trial

Fig. 9 a and b show the absolute ensemble NB and ensemble NRMSE of the estimated regional uptake of ^{227}Th and ^{223}Ra in the lesion, gut, bone, and background in the VIT. Fig. 9 c is a violin plot showing the distribution of the normalized error between the true and estimated uptake for all 60 patients, using the proposed method. The MEW-PDQ method consistently outperformed the DOSEM and GTM-based methods on the task of estimating the uptake of both isotopes in all regions, considering both accuracy and overall error. Note that, the MEW-PDQ method yielded at least 11 times lower ensemble bias in estimating lesion uptake than the compared methods. Further, the absolute ensemble NB obtained with the MEW-PDQ method for both isotopes in all regions was consistently lower than 2.5%. Finally, almost all estimates using the

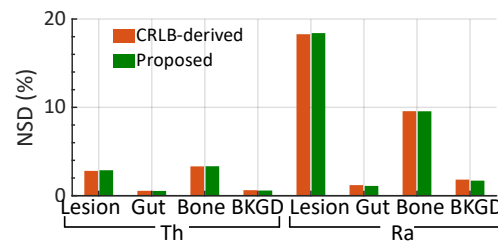


Fig. 8: NSD of the estimated regional uptake of ^{227}Th and ^{223}Ra using the MEW-PDQ method compared with the CRLB-derived NSDs.

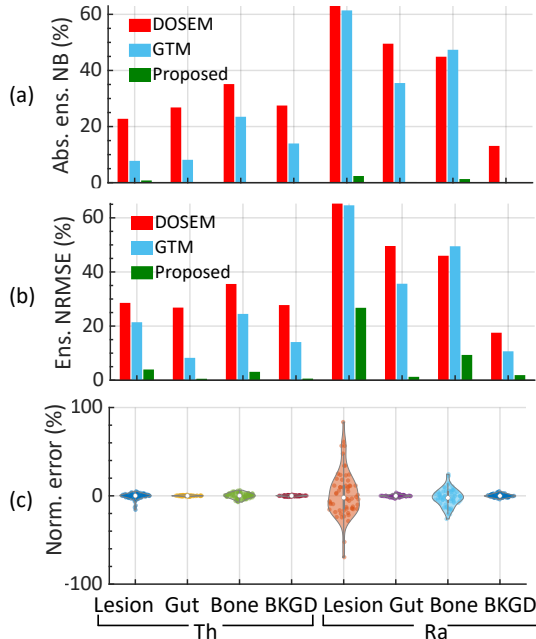


Fig. 9: The (a) absolute ensemble NB and (b) ensemble NRMSE of the estimated uptake of ^{227}Th and ^{223}Ra across different regions using the different methods in the VIT. (c) A violin plot showing the distribution of the normalized error across fifty patients.

proposed method had an error within $\pm 20\%$, except for the lesion uptake of ^{223}Ra , for which 50% of the estimates were within that range.

V. DISCUSSION

We have designed, implemented, and evaluated a MEW-PDQ method to jointly quantify the activity uptake of ^{227}Th and ^{223}Ra with the low-count and crosstalk-contaminated SPECT projections in ^{227}Th -based α -RPTs. The results (Figs. 3-9) demonstrate that the proposed method accurately compensated for the crosstalk contamination of ^{227}Th and ^{223}Ra , effectively addressed the challenges in QSPECT for α -RPTs, including the low counts and complicated SPECT physics, and provided reliable estimates of regional uptake of both isotopes. It also significantly outperformed the compared two state-of-art RBQ methods.

The results in Figs. 3-6 demonstrate that the MEW-PDQ method yielded accurate and precise estimates of lesion uptake of both ^{227}Th and ^{223}Ra with varying lesion characteristics, including different lesion sizes (Fig. 3), LBURs (Fig. 4), ^{227}Th to ^{223}Ra uptake ratios (Fig. 5), and varying levels of spatial inter-lesion heterogeneity (Fig. 6). More specifically, crosstalk contamination and PVEs are two major sources of errors in QSPECT for ^{227}Th -based α -RPT. The low bias of the estimates indicates that the method accurately compensated for the crosstalk contamination. Further, the method was observed to be relatively insensitive to PVEs, as demonstrated by the high accuracy for even small lesion sizes. We note that the DOSEM method is specifically designed to account for the

crosstalk contamination, and the GTM-based method is specifically designed to further compensate for PVEs. However, the proposed method outperformed both approaches. In addition, the proposed method yielded NSD values close to those derived from CRLBs (Figs. 3-5), indicating that the method had the theoretically highest possible precision as an unbiased estimator. This high precision of the method is especially significant given the low counts of α -RPT SPECT. Further, these results indicate that the MEW-PDQ method may be an efficient estimator. Note that if an efficient estimator exists, the ML estimator is efficient [35] and the proposed method is an ML estimator.

An important feature of the MEW-PDQ method is the use of multiple energy windows in quantification. As theoretically shown through the application of the data-processing inequality, discarding projections in one or more energy windows decreases the Fisher information for estimating parameters from the acquired data [31]. This theoretical finding is manifested in our results in Fig. 7, where we see that using data from multiple energy windows significantly reduces the CRLB. This further motivates the need to develop QSPECT methods that can use data from multiple energy windows, such as the proposed method. This is particularly crucial for α -particle SPECT, as the low number of detected counts can be increased by including data from multiple energy windows. Further, as shown in Fig. 8, using projections in all four energy windows, the variance of estimates obtained by the proposed method approached the corresponding CRLB for all VOIs and both isotopes. This finding demonstrates the effectiveness of the proposed method in utilizing information from all four energy windows. Thus, these results demonstrate the efficacy obtained by using multiple energy windows as enabled by the proposed method.

The efficacy of the proposed method was also observed in a VIT. We see that the MEW-PDQ method yielded averaged absolute ensemble NB and ensemble NRMSE values as low as 0.6% and 5.9%, respectively (Fig. 9). In contrast, the DOSEM-based method yielded corresponding average absolute ensemble NB and ensemble NRMSE of 35.3% and 37.1%, respectively. The GTM-based method yielded corresponding values of 24.7% and 28.6%, respectively. These observations for the DOSEM and GTM-based method are consistent with previous literature [24]–[28] and confirm the limitation of these conventional approaches for the task of joint ^{227}Th and ^{223}Ra regional uptake quantification. These results further demonstrate the reliability and superiority of the proposed MEW-PDQ method for this task.

The proposed MEW-PDQ method, unlike reconstruction-based quantification methods, directly estimates the mean regional uptake from the projection data. In this process, the method does not specifically account for any spatial heterogeneity in uptake within a VOI. However, results in Fig. 6 show that such heterogeneity did not significantly affect the reliability of the estimates. Notably, even in the presence of such heterogeneity, the proposed method outperforms the DOSEM and GTM-based approaches, suggesting that the MEW-PDQ method may still be a reliable and superior option.

For dosimetry studies with systematically administered ra-

dionuclide therapies, the patients are typically imaged at multiple time points post-administration. Due to the decay of ^{227}Th to ^{223}Ra , there will be different ^{227}Th to ^{223}Ra uptake ratios in the patient at those time points. Fig. 5 shows the reliable and superior performance of the MEW-PDQ method to estimate the regional uptake of both isotopes with all ^{227}Th to ^{223}Ra uptake ratios. These results motivate further evaluation of the method for ^{227}Th -based α -RPT dosimetry studies.

The MC-based approach generated system matrix of the proposed method allows for accurate modeling and compensation of crosstalk contamination and the other complicated SPECT physics in ^{227}Th -based α -RPTs. This MC-based approach was relatively fast, and the system matrix can be pre-computed and stored given the small number of VOIs. For a typical simulated patient in this study, computing the system matrix of both isotopes for all VOIs took less than 10 minutes on our system equipped with Intel(R) Xeon(R) Gold 6230 CPU with 80 cores. The system matrix required only 120 MB for storage and memory during computation. In contrast, a similar MC-based approach for the DOSEM-based method may produce a system matrix as large as 40 TB for a single patient, which is not feasible for processing and storage with typical computational systems. Additionally, due to the low number of unknowns, the 1000 iterations of the MEW-PDQ method required less than 10 minutes on a desktop computer with a 16-core Intel Core i7-10700K CPU. Thus, the proposed method has the capability to efficiently perform system matrix modeling and regional uptake estimation with modest computational requirements.

The tradeoff with the MEW-PDQ method is that the method quantifies regional uptake rather than voxel values, which precludes estimating dose-volume histograms for VOIs such as the lesion. However, given the low counts for α -RPT SPECT, the reconstructed images are inherently very noisy. The dose-volume histogram may not be feasible to compute even with an RBQ method and thus, a more viable goal is to estimate regional uptake. In that context, the MEW-PDQ method demonstrates its reliability.

A further limitation of this study is that the proposed method was evaluated with simulations. Although we simulated realistic patient phantoms and validated our SPECT system simulations with physical phantoms, there may be mismatches in simulating the patient population variabilities and system instrumentation. Also, due to the absence of reliable radiopharmacokinetic data, we modeled the regional uptake ratios of ^{227}Th based on clinical studies using ^{223}Ra . Additionally, the biological half-life of these isotopes was not considered in the experiments that evaluated the performance of the proposed method at various ^{227}Th to ^{223}Ra uptake ratios. Evaluation of the method with physical phantoms and patient data, including data from ongoing clinical trials such as NCT03724747, provides a mechanism to address these limitations. The results from this study strongly motivate further validation of the proposed method with physical phantom and clinical data.

VI. CONCLUSION

We proposed a multiple-energy-window projection-domain quantitative SPECT (MEW-PDQ) method for joint regional uptake quantification of ^{227}Th and ^{223}Ra . The method was observed to yield reliable (accurate and precise) estimates of the regional uptake of both isotopes, as evaluated using clinically realistic and validated simulation studies in the context of ^{227}Th -based α -RPT, for multiple variations in lesion properties. This included variations in lesion sizes, lesion-to-bone uptake ratios, ^{227}Th to ^{223}Ra uptake ratios, and different levels of spatial intra-lesion heterogeneity. The proposed method consistently outperformed reconstruction-based quantification approaches including a dual-isotope ordered subset expectation maximization (DOSEM)-based method and a geometric transfer matrix (GTM)-based method. We also observed that the proposed method yielded estimates that were almost unbiased and had a standard deviation close to that derived from the Cramér-rao lower bound, indicating that the method may be an efficient estimator. Moreover, by enabling the use of data from multiple energy windows, the proposed method was observed to yield highly precise activity uptake estimates, with the variance of these estimates approaching the Cramér-rao lower bound. Further, in a virtual imaging trial, the proposed method yielded reliable estimates and outperformed both the DOSEM and GTM-based methods. Overall, the results provide strong evidence supporting further evaluation and application of this method for performing quantitative SPECT of ^{227}Th -based α -RPTs.

ACKNOWLEDGMENT

We thank the Washington University Center for High Performance Computing for providing computational resources for this project. The center is partially funded by National Institutes of Health (NIH) grants 1S10RR022984-01A1 and 1S10OD018091-01. All authors declare that they have no known conflicts of interest in terms of competing financial interests or personal relationships that could have an influence or are relevant to the work reported in this paper.

REFERENCES

- [1] J. Baranowska-Kortylewicz, J. G. Sharp, T. R. McGuire, S. Joshi, and D. W. Coulter, "Alpha-Particle Therapy for Multifocal Osteosarcoma: A Hypothesis," *Cancer Biother Radiopharm*, vol. 35, no. 6, pp. 418–424, 2020.
- [2] V. Frantellizzi *et al.*, "Targeted alpha therapy with thorium-227," *Cancer Biother Radiopharm*, vol. 35, no. 6, pp. 437–445, 2020.
- [3] U. B. Hagemann *et al.*, "Advances in precision oncology: targeted thorium-227 conjugates as a new modality in targeted alpha therapy," *Cancer Biother Radiopharm*, vol. 35, no. 7, pp. 497–510, 2020.
- [4] N. K. Tafreshi *et al.*, "Development of targeted alpha particle therapy for solid tumors," *Molecules*, vol. 24, no. 23, p. 4314, 2019.
- [5] J.-P. Pouget *et al.*, "Clinical radioimmunotherapy—the role of radiobiology," *Nature reviews Clinical oncology*, vol. 8, no. 12, pp. 720–734, 2011.
- [6] E. Larsson, G. Brodin, A. Cleton, T. Ohlsson, O. Lindén, and C. Hindorf, "Feasibility of thorium-227/radium-223 gamma-camera imaging during radionuclide therapy," *Cancer Biother Radiopharm*, vol. 35, no. 7, pp. 540–548, 2020.
- [7] B. Brans *et al.*, "Clinical radionuclide therapy dosimetry: the quest for the "Holy Gray"," *Eur J Nucl Med Mol Imaging*, vol. 34, no. 5, pp. 772–786, 2007.

- [8] E. Garin *et al.*, “Personalised versus standard dosimetry approach of selective internal radiation therapy in patients with locally advanced hepatocellular carcinoma (DOSISPHERE-01): a randomised, multicentre, open-label phase 2 trial,” *Lancet Gastroenterol Hepatol*, vol. 6, no. 1, pp. 17–29, 2021.
- [9] J. A. Siegel *et al.*, “Red marrow radiation dose adjustment using plasma FLT3-L cytokine levels: improved correlations between hematologic toxicity and bone marrow dose for radioimmunotherapy patients,” *J Nucl Med*, vol. 44, no. 1, pp. 67–76, 2003.
- [10] G. Sgouros, “Dosimetry, radiobiology and synthetic lethality: radiopharmaceutical therapy (RPT) with alpha-particle-emitters,” in *Semin Nucl Med*, vol. 50, no. 2. Elsevier, 2020, pp. 124–132.
- [11] I. Murray, B. Rojas, J. Gear, R. Callister, A. Cleton, and G. D. Flux, “Quantitative Dual-Isotope Planar Imaging of Thorium-227 and Radium-223 Using Defined Energy Windows,” *Cancer Biother Radiopharm*, vol. 35, no. 7, pp. 530–539, 2020.
- [12] T. Ichihara, K. Ogawa, N. Motomura, A. Kubo, and S. Hashimoto, “Compton scatter compensation using the triple-energy window method for single-and dual-isotope SPECT,” *J Nucl Med*, vol. 34, no. 12, pp. 2216–2221, 1993.
- [13] S. C. Moore *et al.*, “Simultaneous Tc-99m/Tl-201 imaging using energy-based estimation of the spatial distributions of contaminant photons,” *IEEE Trans Nucl Sci*, vol. 42, no. 4, pp. 1189–1195, 1995.
- [14] J. M. Links, J. L. Prince, and S. N. Gupta, “A vector Wiener filter for dual-radionuclide imaging,” *IEEE Trans Med Imaging*, vol. 15, no. 5, pp. 700–709, 1996.
- [15] J. Feng and B. C. Penney, “Accurate spill-down and scatter correction for Tc-99m/In-111 SPECT,” in *2002 IEEE Nucl Sci Symp Conf Rec*, vol. 3. IEEE, 2002, pp. 1562–1566.
- [16] Y. Du, B. M. Tsui, and E. C. Frey, “Model-based crosstalk compensation for simultaneous dual-isotope brain SPECT imaging,” *Med Phys*, vol. 34, no. 9, pp. 3530–3543, 2007.
- [17] M. King, D. Devries, T.-S. Pan, P. Pretorius, and J. Case, “An investigation of the filtering of TEW scatter estimates used to compensate for scatter with ordered subset reconstructions,” *IEEE Transactions on Nuclear Science*, vol. 44, no. 3, pp. 1140–1145, 1997.
- [18] D. J. Kadrmaz, E. C. Frey, and B. M. Tsui, “Simultaneous technetium-99m/thallium-201 SPECT imaging with model-based compensation for cross-contaminating effects,” *Phys Med Biol*, vol. 44, no. 7, p. 1843, 1999.
- [19] W. Wang, E. Frey, B. Tsui, and C. Tocharoenchai, “A model-based crosstalk compensation method for simultaneous Tl-201 and Tc-99m dual isotope myocardial SPECT imaging,” in *2001 IEEE Nucl Sci Symp Conf Rec (Cat. No. 01CH37310)*, vol. 4. IEEE, 2001, pp. 2209–2213.
- [20] X. Song, E. Frey, W. Wang, Y. Du, and B. Tsui, “Validation and evaluation of model-based crosstalk compensation method in simultaneous/sup 99mTc stress and/sup 201Tl rest myocardial perfusion SPECT,” *IEEE Trans Nucl Sci*, vol. 51, no. 1, pp. 72–79, 2004.
- [21] Y. Du and E. C. Frey, “Quantitative evaluation of simultaneous reconstruction with model-based crosstalk compensation for dual-isotope simultaneous acquisition brain SPECT,” *Med Phys*, vol. 36, no. 6Part1, pp. 2021–2033, 2009.
- [22] H. De Jong, F. Beekman, M. Viergever, and P. Van Rijk, “Simultaneous 99mTc/201Tl dual-isotope SPET with Monte Carlo-based down-scatter correction,” *Eur J Nucl Med Mol Imaging*, vol. 29, no. 8, pp. 1063–1071, 2002.
- [23] J. Ouyang, G. El Fakhri, S. C. Moore, and M. F. Kijewski, “Fast Monte Carlo Simulation Based Joint Iterative Reconstruction for Simultaneous 99mTc/123I Brain SPECT Imaging,” in *2006 IEEE Nucl Sci Symp Conf Rec*, vol. 4. IEEE, 2006, pp. 2251–2256.
- [24] M. Ghaly, G. Sgouros, and E. Frey, “Quantitative Dual Isotope SPECT Imaging of the alpha-emitters Th-227 and Ra-223,” *J Nucl Med*, vol. 60 (supplement 1), pp. 41–41, 2019.
- [25] Z. Li *et al.*, “A Projection-Domain Low-Count Quantitative SPECT Method for α -Particle-Emitting Radiopharmaceutical Therapy,” *IEEE Transactions on Radiation and Plasma Medical Sciences*, vol. 7, no. 1, pp. 62–74, 2023.
- [26] N. Benabdallah, M. Bernardini, M. Bianciardi, C. de Labriolle-Vaylet, D. Franck, and A. Desbrée, “²²³Ra-dichloride therapy of bone metastasis: optimization of SPECT images for quantification,” *EJNMMI Res*, vol. 9, no. 1, pp. 1–12, 2019.
- [27] J. Yue, R. Hobbs, G. Sgouros, and E. Frey, “SU-F-J-08: Quantitative SPECT Imaging of Ra-223 in a Phantom,” *Med Phys*, vol. 43, no. 6Part8, pp. 3407–3407, 2016.
- [28] J. Gustafsson, E. Rodeño, and P. Mínguez, “Feasibility and limitations of quantitative SPECT for ²²³Ra,” *Phys Med Biol*, vol. 65, no. 8, p. 085012, 2020.
- [29] R. E. Carson, “A maximum likelihood method for region-of-interest evaluation in emission tomography,” *J Comput Assist Tomogr*, vol. 10, no. 4, pp. 654–663, 1986.
- [30] M. A. Rahman, R. Laforest, and A. K. Jha, “A list-mode OSEM-based attenuation and scatter compensation method for SPECT,” in *Proc IEEE 17th Int Symp Biomed Imaging*. IEEE, 2020, pp. 646–650.
- [31] S. Y. Chun, M. P. Nguyen, T. Q. Phan, H. Kim, J. A. Fessler, and Y. K. Dewaraja, “Algorithms and Analyses for Joint Spectral Image Reconstruction in Y-90 Bremsstrahlung SPECT,” *IEEE Trans Med Imaging*, vol. 39, no. 5, pp. 1369–1379, 2019.
- [32] Z. Li, N. Benabdallah, R. Laforest, R. Wahl, D. Thorek, and A. Jha, “A multiple-energy-window projection-domain quantitative SPECT method for joint regional uptake quantification of Thorium-227 and Radium-223,” pp. 2399–2399, 2022. [Online]. Available: https://jnm.snmjournals.org/content/63/supplement_2/2399
- [33] G. Schramm, A. Rezaei, K. Thielemans, and J. Nuyts, “Proceedings of the 16th Virtual International Meeting on Fully 3D Image Reconstruction in Radiology and Nuclear Medicine,” *arXiv preprint arXiv:2110.04143*, pp. 58–61, 2021.
- [34] M. Soret, S. L. Bacharach, and I. Buvat, “Partial-volume effect in PET tumor imaging,” *J Nucl Med*, vol. 48, no. 6, pp. 932–945, 2007.
- [35] H. H. Barrett and K. J. Myers, *Foundations of image science*. John Wiley & Sons, 2013.
- [36] N. J. Beaudry and R. Renner, “An intuitive proof of the data processing inequality,” *arXiv preprint arXiv:1107.0740*, 2011.
- [37] M. Ljungberg and S.-E. Strand, “A Monte Carlo program for the simulation of scintillation camera characteristics,” *Comput Methods Programs Biomed*, vol. 29, no. 4, pp. 257–272, 1989.
- [38] M. B. Toossi, J. P. Islamian, M. Momenzad, M. Ljungberg, and S. Naseri, “SIMIND Monte Carlo simulation of a single photon emission CT,” *J Med Phys*, vol. 35, no. 1, p. 42, 2010.
- [39] M. Morphis, J. A. van Staden, H. du Raan, and M. Ljungberg, “Validation of a SIMIND Monte Carlo modelled gamma camera for Iodine-123 and Iodine-131 imaging,” *Heliyon*, vol. 7, no. 6, p. e07196, 2021.
- [40] Z. Li, N. Benabdallah, R. Laforest, R. Wahl, D. Thorek, and A. Jha, “Joint regional uptake quantification of ²²⁷Th and ²²³Ra using a multiple-energy-window projection-domain quantitative SPECT method,” available online at https://github.com/ajha4/Alpha-SPECT/blob/main/MEW_PDQ_Supplementary.pdf, Feb. 2023.
- [41] W. P. Segars, M. Mahesh, T. J. Beck, E. C. Frey, and B. M. Tsui, “Realistic CT simulation using the 4D XCAT phantom,” *Med Phys*, vol. 35, no. 8, pp. 3800–3808, 2008.
- [42] O. G. Rousset, Y. Ma, and A. C. Evans, “Correction for partial volume effects in PET: principle and validation,” *J Nucl Med*, vol. 39, no. 5, pp. 904–911, 1998.
- [43] I. Murray *et al.*, “The potential of ²²³Ra and ¹⁸F-fluoride imaging to predict bone lesion response to treatment with ²²³Ra-dichloride in castration-resistant prostate cancer,” *Eur J Nucl Med Mol Imaging*, vol. 44, no. 11, pp. 1832–1844, 2017.
- [44] D. S. Abou, D. Ulmert, M. Doucet, R. F. Hobbs, R. C. Riddle, and D. L. Thorek, “Whole-body and microenvironmental localization of radium-223 in naive and mouse models of prostate cancer metastasis,” *J Natl Cancer Inst*, vol. 108, no. 5, p. djv380, 2016.
- [45] D. S. Abou *et al.*, “Preclinical single photon emission computed tomography of alpha particle-emitting radium-223,” *Cancer Biother Radiopharm*, vol. 35, no. 7, pp. 520–529, 2020.
- [46] Z. Liu *et al.*, “Observer study-based evaluation of a stochastic and physics-based method to generate oncological PET images,” in *Medical Imaging 2021: Image Perception, Observer Performance, and Technology Assessment*, vol. 11599. International Society for Optics and Photonics, 2021, p. 1159905.
- [47] E. Abadi *et al.*, “Virtual clinical trials in medical imaging: a review,” *J Med Imaging*, vol. 7, no. 4, p. 042805, 2020.
- [48] T. Merlin *et al.*, “CASToR: a generic data organization and processing code framework for multi-modal and multi-dimensional tomographic reconstruction,” *Phys Med Biol*, vol. 63, no. 18, p. 185005, 2018.
- [49] E. C. Frey and B. Tsui, “A new method for modeling the spatially-variant, object-dependent scatter response function in SPECT,” in *1996 IEEE Nucl Sci Symp Conf Rec*, vol. 2. IEEE, 1996, pp. 1082–1086.

Supplementary Materials

S-I. IMAGE RECONSTRUCTION-BASED METHODS COMPARED

A. Dual-isotope ordered subset expectation maximization image reconstruction (DOSEM)-based method

Based on analysis of the emission spectra of both isotopes, energy windows 1 and 3 were considered as the primary energy windows of ^{223}Ra and ^{227}Th , respectively. We first reconstructed images of activity uptake of ^{227}Th and ^{223}Ra using projections from the corresponding two separate primary energy windows. In this step, we assumed there was no crosstalk contamination, i.e., the counts in the two energy windows solely reflected emissions from ^{227}Th and ^{223}Ra , respectively. The images were reconstructed using the ordered subset expectation maximization (OSEM) method, implemented using Customizable and Advanced Software for Tomographic Reconstruction (CASToR) software [48]. In this process, we compensated for attenuation, scatter, collimator-detector response, stray-radiation-related noise, and the complicated emission spectra of both isotopes. The scatter was compensated using effective scatter source estimation (ESSE) method [49]. Next, the reconstructed image of each isotope was forward projected to the photopeak energy window of the other isotope to estimate the crosstalk contamination in each photopeak energy window. In this forward projection, we modeled the emission spectra of both isotopes, attenuation, scatter, and collimator-detector response. In this step, the crosstalk contamination from primary photons was modeled from the emission spectrum, and the crosstalk contamination from scattered photons was modeled with the ESSE method. Then, the images of both isotopes were again reconstructed using the OSEM method, with the estimated crosstalk contamination as additive correction terms. Since the estimates of crosstalk contamination were not accurate due to the inaccurate reconstruction in the first step, we repeated these steps for multiple iterations until the changes in the reconstructed images were small.

B. Geometric transfer matrix (GTM)-based method

PVEs are known to degrade quantification accuracy in SPECT [34]. The MEW-PDQ method implicitly assumes constant uptake within each VOI. Under this assumption, PVEs can also be compensated for post-reconstruction. We compared our approach to the widely used GTM-based method [42], calculating the elements of the GTM from the reconstructed projections of the VOIs for each isotope. Additional implementation details of this method are described in [42].

S-II. FIGURES OF MERIT

For a range of experimental conditions, we generated multiple instances of projection data for a single phantom, where each instance corresponded to separate noise realizations. Denote the total number of realizations by R . Considering one of the isotopes, denote the true activity uptake of the

k^{th} VOI by λ_k and the corresponding estimate with the r^{th} noise realization by $\hat{\lambda}_{rk}$. In these experiments, the accuracy of the estimated uptake of this isotope was quantified using the normalized bias (NB), which, for the k^{th} VOI, is given by

$$\text{NB}_k = \frac{1}{R} \sum_{r=1}^R \frac{\hat{\lambda}_{rk} - \lambda_k}{\lambda_k}. \quad (20)$$

The precision of the estimated uptake of this isotope was quantified using the normalized standard deviation (NSD), which, for the k^{th} VOI, is given by

$$\text{NSD}_k = \sqrt{\frac{1}{R-1} \sum_{r=1}^R \left(\frac{\hat{\lambda}_{rk}}{\lambda_k} - \frac{1}{R} \sum_{r'=1}^R \frac{\hat{\lambda}_{r'k}}{\lambda_k} \right)^2}. \quad (21)$$

Finally, the overall error in estimating the uptake was quantified by the normalized root mean square error (NRMSE). For the k^{th} VOI,

$$\text{NRMSE}_k = \sqrt{\text{NB}_k^2 + \text{NSD}_k^2}. \quad (22)$$

To evaluate the performance of the methods over populations, we used the ensemble NB and ensemble NRMSE. We denote the number of samples in the population by S and denote the true and estimated activity uptake of a particular isotope in the k^{th} VOI for the s^{th} sample by λ_{sk} and $\hat{\lambda}_{sk}$, respectively. The ensemble NB for the k^{th} VOI is given by

$$\text{Ensemble NB}_k = \frac{1}{S} \sum_{s=1}^S \frac{\hat{\lambda}_{sk} - \lambda_{sk}}{\lambda_{sk}}. \quad (23)$$

The ensemble NRMSE for the k^{th} VOI is given by

$$\text{Ensemble NRMSE}_k = \sqrt{\frac{1}{S} \sum_{s=1}^S \left(\frac{\hat{\lambda}_{sk} - \lambda_{sk}}{\lambda_{sk}} \right)^2}. \quad (24)$$

Additionally, to quantify performance in cases where we had just a single estimate, we used normalized error, defined as the difference between the true and estimated uptake values, normalized by the true uptake value.

Finally, we also computed the Cramér-Rao lower bound (CRLB), which is the minimum variance that can be achieved by an unbiased estimator, as a benchmark for the precision of the activity estimated using the proposed method. The CRLB is given by the diagonal elements of the inverse of the Fisher information matrix for the estimated parameter. We denote the Fisher information matrix by \mathbf{F} [35]. Since the proposed method estimates the regional uptake of ^{227}Th and ^{223}Ra at the same time, the Fisher information matrix needs to consider both isotopes. We denoted λ_l and $\hat{\lambda}_l$ as the true and estimated activity uptake respectively, where l ranges over the two isotopes in K VOIs. Thus the Fisher information matrix is a $2K$ by $2K$ matrix with elements given by

$$F_{l_1 l_2} = -E \left[\frac{\partial^2}{\partial \lambda_{l_1} \partial \lambda_{l_2}} \ln \Pr(\mathbf{g}|\boldsymbol{\lambda}) \right]. \quad (25)$$

We have already derived the likelihood of the measured data \mathbf{g} in the main material:

$$\Pr(\mathbf{g}|\boldsymbol{\lambda}) = \prod_{m=1}^M \exp[-(\mathbf{H}\boldsymbol{\lambda})_m - \psi_m] \frac{[(\mathbf{H}\boldsymbol{\lambda})_m + \psi_m]^{g_m}}{g_m!}. \quad (26)$$

Substituting Eq. (26) in Eq. (25) yields

$$F_{l_1 l_2} = \sum_{m=1}^M \frac{H_{ml_1} H_{ml_2}}{(\mathbf{H}\boldsymbol{\lambda})_m + \psi_m}. \quad (27)$$

S-III. VALIDATING THE SPECT SIMULATION

A. Experiments

SIMIND is a MC approach that has already been shown to model SPECT imaging systems accurately [37]–[39], including when imaging other α -particle isotopes [25]. To demonstrate the accuracy of the SIMIND-based simulation approach for ^{227}Th -based α -RPT SPECT, we compared the projection data obtained with our simulation approach to that obtained on a physical scanner. For this purpose, we used a NEMA phantom (Data SpectrumTM, USA). The spheres of this phantom were filled with ^{227}Th solutions with an activity concentration of 40 kBq/ml. The rest of the phantom was filled with water to simulate attenuation and scatter due to soft tissue. The phantom was scanned on a GE Discovery 670 SPECT/CT system with a medium energy general purpose (MEGP) collimator one day after purifying the ^{227}Th isotope and filling the isotope in the phantom. Thus, at the time of scanning, a small portion of the ^{227}Th had decayed to ^{223}Ra . During imaging, projections were acquired in two energy windows, corresponding to the two major photopeaks of ^{223}Ra (66 - 98 keV) and ^{227}Th (217 - 260 keV) at 60 angular positions spaced uniformly over 360° . This image-acquisition process was modeled using our simulation approach. In the simulation, the concentration of ^{227}Th and ^{223}Ra were calculated theoretically, based on the filling and scanning time. The profiles of the projection data obtained with the physical scanner and with the simulation approach from the two energy windows were compared.

B. Results

Fig. 10 shows projections of the NEMA phantom in the two energy windows at the first angular position, acquired using simulated and physical SPECT systems. We also compared the profiles along the dashed line in the projections from the two approaches in both energy windows. To reduce the noise-related variation in this profile, each point in the profile was obtained by averaging the number of counts along five adjacent pixels on both sides of the dashed line. We observed that the profile of the simulated projection matched that acquired on the physical scanner in both energy windows. This provides evidence of the accuracy of the process to simulate isotope emission, the SPECT system, and the noise in this study.

S-IV. THE 3D LUMPY MODEL USED TO SIMULATE INTRA-LESION HETEROGENEITY

Denote the support of the lesion in the object space by $s(\mathbf{r})$. Then, the lesion activity uptake, denoted by $f_l(\mathbf{r})$, is given by

$$f_l(\mathbf{r}) = s(\mathbf{r}) \sum_{p=1}^P \frac{a_p}{2\pi\sigma_p^2} \exp\left(-\frac{|\mathbf{r} - \mathbf{c}_p|^2}{\sigma_p^2}\right), \quad (28)$$

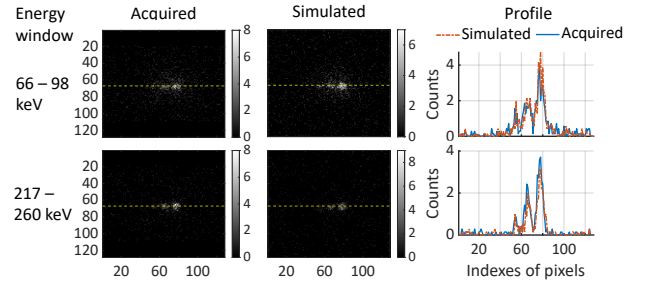


Fig. 10: Comparison of the simulated and physical-SPECT-system-acquired projections of the NEMA phantom in two different energy windows.

where P denotes the total number of lumps, and \mathbf{c}_p , a_p , and σ_p denote the center, magnitude, and width of the p^{th} lump function, respectively. Different levels of heterogeneity were simulated by varying the values of P , \mathbf{c}_p , a_p , and σ_p .